Interfacial Dynamics of Two Liquids Under an Oscillating Gravitational Field

Walter M. B. Duval* and David A. Jacqmin*
NASA Lewis Research Center, Cleveland, Ohio 44135

The evolution of two miscible liquids meeting at an initially sharp interface inside a cavity under microgravity g-jitter conditions is studied numerically. We show the response of the interface and kinematics of the flowfield to various g-jitter accelerations and aspect ratio variations. The interface region acts like a vortex source sheet, and it can be unstable to Kelvin-Helmholtz and Rayleigh-Taylor instabilities. The vortices produced along the interface can serve as a stirring mechanism to promote local mixing. Below the critical Stokes-Reynolds number, the destabilization of the interface results in deformation into wavy structures. In some parameter regions, these structures oscillate in time; in others, they are quasisteady. Above the critical Stokes-Reynolds number, "chaotic" instability results and the interface breaks into concentration pockets. The morphology of the initial breakup is similar to observed Rayleigh-Taylor instability. Subsequent mixing of the two fluids after the breakup of the interface is then very rapid.

Nomenclature

$\mathcal{R}$ = aspect ratio
C = dimensionless species, $C^* - C_r^*/C_l^* - C_r^*$
$\bar{D}_{lr}$ = molecular mass diffusion coefficient
Gr = Grashof number, $(\Delta\rho/\bar{\rho})\ (ng_oH^3/\bar{\nu}^2)$
g = gravitational acceleration
H = cavity height
j = unit vector in vertical direction
L = cavity width
n = normal vector to cavity
n = ratio
Pe_D = Peclect number based on mass diffusion
q = distance from mesh points normal to the cavity wall
Re = Reynolds number
Re_s = Stokes-Reynolds number
Sc = Schmidt number, $\bar{\nu}/\bar{D}_{lr}$
T = period of oscillation
t = dimensionless time, t^*/T
U_c = characteristic velocity, $(\Delta\rho/\bar{\rho})$, (ng_o/ω)
u, v = dimensionless velocity in x and y directions, $u^*/U_c = \partial\Psi/\partial y$, $v^*/U_c = -\partial\Psi/\partial x$
x,y = dimensionless horizontal and vertical direction, x^*/L, y^*/H
β = isothermal coefficient of concentration expansivity
Γ = boundary cavity
Δ = difference
δ_s = Stokes length scale
ζ = dimensionless vorticity, $\zeta^* H/U_c = (\mathcal{R}\partial v/\partial x) - (\partial u/\partial y)$
$\bar{\nu}$ = average kinematic viscosity, $(\nu_l + \nu_r)/2$
ρ = density
τ = dimensionless oscillation time, $t/2\pi$
Ψ = dimensionless stream function, Ψ^*/U_cH
ω = circular frequency
∇ = gradient in x and y directions
∇^2 = Laplacian in two directions

Superscripts
* = dimensionless quantity
− = average quantity

Subscripts
c = characteristic value
D = length scale based on mass diffusion
l = left side
o = reference to Earth
r = right side
s = length scale based on viscosity
w = mesh points

Introduction

THEORETICAL efforts aimed at explaining the effects of the gravitational field on materials processing conducted inside a Space Shuttle environment[1] have focused on the analysis of convection inside differentially heated enclosures. These studies show that the gravitational field can be resolved into a mean and a fluctuating component. The fluctuating component, often referred to as "g-jitter," can be important in affecting materials processing. Kamotoni et al.[2] studied the effect of g-jitter on thermal convection inside an enclosure. They show that g-jitter can be effective in generating thermal convection, and the resulting flows are oscillatory with very small displacements.

A particular application of great current interest in solution crystal growth, as discussed by Galster and Nielsen[3] and Gerbi et al.,[4] is the process of opposite oriented diffusion growth. This process for crystal growth was carried out under both ground-based conditions on Earth and the microgravity environment inside a Space Shuttle. In this method of crystal growth, multiple chambers filled with fluids of different compositions separated by valve arrangements are used to achieve the growth of the desired crystal. The level of convection present, caused by the gravitational field, affects the pattern of dislocations on the grown crystals. For the ground-based experiments of Galster and Nielsen,[3] suppression of gravity induced convection was achieved by placing fibers between the chambers. The results of their space experiments showed that the experimental setups where filters used between the chambers gave higher quality crystals than the ones that had no filters. This indicated that, even in space, excessive levels of g-jitter could be present. Alternative methods for suppressing convection involve the use of gels,[5] however, impurities and imperfections are then introduced in the grown crystals.

Recently, after a series of experiments were conducted in space that used an experimental apparatus with multiple chambers similar to that of Galster and Nielsen, Radcliffe et al.[6]

Received Aug. 22, 1988; revision received Jan. 23, 1990.

*Physicist.

analyzed the effects of the gravitational field on both counter-diffusion solution crystal growth and on fluid mixing for both large and small density differences. Their crystal growth experiments did not yield superior crystals to those grown on Earth. The fluid mixing experiments involving large density differences showed that convective mixing occurred, whereas those with low density differences indicated negligible effects due to convection. The dominant mechanism for low density difference liquid mixing was hypothesized to be long time scale mass diffusion. However, the results for both the crystal growth experiments and the large density difference fluid experiments were unexpected because of the expected low gravitational field in space. These unexpected results were attributed to the overwhelming effects of g-jitter.

The purpose of this investigation is to examine the effect of g-jitter typical of the Space Shuttle environment on the mixing characteristics of two miscible liquids with no surface tension, which initially meet at a sharp interface. We consider both small and large density differences in our parametric studies. This brackets many liquid pairs that mix ideally[7-9] with no heat generation. We show that the transient evolution of the liquid-liquid interface exhibits trends that can be characterized as either stable or unstable to the input forcing gravitational field. On the one hand, though convection is present for the stable case, the interface remains sharp and undeformed over the time considered. Long time scale mixing, for the stable very low density difference case, is dominated by mass diffusion. On the other hand, two types of interfacial instabilities are identified for the large density difference cases: the classical Kelvin-Helmholtz instability,[10,11] which results in growth and oscillation of the interface, and "chaotic" instability associated with interfacial breakup. Because of the discontinuity associated with the initial condition at the interface, it behaves like a vortex sheet as it evolves, and it displays many features discussed in the works of Rosenhead,[12] Zalosh,[13] Rottman and Olfe,[14] and more recently by Krazny.[15] These features include the influence of vortex concentration on the interface shape, vortex rollup, and breaking waves. Paths to chaotic instability are shown to be associated with continuous growth and deformation of the interface leading to Rayleigh-Taylor instability, and finally breaking into concentration pockets with a large number of vortices distributed in the flow that give rise to a vigorous mechanism for mixing.

To get a full scope on the effects of convection on mass transport under microgravity conditions, in addition to a full parametric study on square cavities of various sizes, we also consider both high- and low-aspect ratios. We show the effect of both amplitude and frequency variation. Lastly, we study the evolution of the interface leading to chaotic instability, and show when breakup of the interface occurs and chaotic mixing ensues.

Formulation

The mixing characteristics of two fluids under g-jitter conditions are studied by adopting the initial condition in Fig. 1. The two fluids components are in contact at the centerline. The higher and lower density fluids are, respectively, on the left and right sides of the cavity. They are subjected to a sinusoidal gravitational field that is oriented in the vertical direction. For an isothermal system, the resulting flow may be approximated mathematically by the Boussinesq equations:

$$\nabla \cdot V^* = 0 \tag{1}$$

$$\tilde{\rho}\frac{DV^*}{Dt^*} = -\nabla p^* + \tilde{\mu}\nabla^2 V^* + \rho g(t^*) \tag{2}$$

$$\frac{DC^*}{Dt^*} = \tilde{D}_{lr}\nabla^2 C^* \tag{3}$$

where

$$\rho = \tilde{\rho}(1 + \beta \Delta C) \tag{4}$$

$$\beta = \frac{1}{\tilde{\rho}}\frac{\partial \rho}{\partial C} \tag{5}$$

$$g(t^*) = ng_o \cos(\omega t^*)j \tag{6}$$

with the following initial and boundary conditions

$$t^* = 0 \qquad C^*(x,y,t) = \begin{cases} 1 & \le x < L/2 \\ 0.5 & x = L/2 \\ 0 & L/2 < x \le L \end{cases} \tag{7}$$

$$t^* > 0 \qquad V = 0 \text{ on } \Gamma, \text{ no slip}$$

$$\nabla C^* n = 0 \text{ on } \Gamma, \text{ condition of impermeability}$$

In the preceding equations, the viscosity and mass molecular diffusion coefficient are approximated to be independent of concentration. Over the interface region, the viscosity and density are averaged.

The two components of the momentum equation may be combined into one equation by using the vorticity-stream function relationships. We use the geometric dimensions of the cavity of length scales, and the frequency of the oscillating gravitational field for time scale. The characteristic velocity is based on the ratio of buoyancy to input frequency. The resulting equations may be cast into dimensionless form to obtain the following equations:

$$\mathcal{A}^2\frac{\partial^2 \Psi}{\partial x^2} + \frac{\partial^2 \Psi}{\partial y^2} = -\zeta \tag{8}$$

$$\frac{\partial \zeta}{\partial t} + \frac{Gr}{Re^2}\left(\mathcal{A}\, u\frac{\partial \zeta}{\partial x} + v\frac{\partial \zeta}{\partial y}\right) = \frac{1}{Re}\left(\mathcal{A}^2\frac{\partial^2 \zeta}{\partial x^2} + \frac{\partial^2 \zeta}{\partial y^2}\right) + \mathcal{A}\frac{\partial C}{\partial x}\cos t \tag{9}$$

$$\frac{\partial C}{\partial t} + \frac{Gr}{Re^2}\left(\mathcal{A}\, u\frac{\partial C}{\partial x} + v\frac{\partial C}{\partial y}\right) = \frac{1}{Pe_D}\left(\mathcal{A}^2\frac{\partial^2 C}{\partial x^2} + \frac{\partial^2 C}{\partial y^2}\right) \tag{10}$$

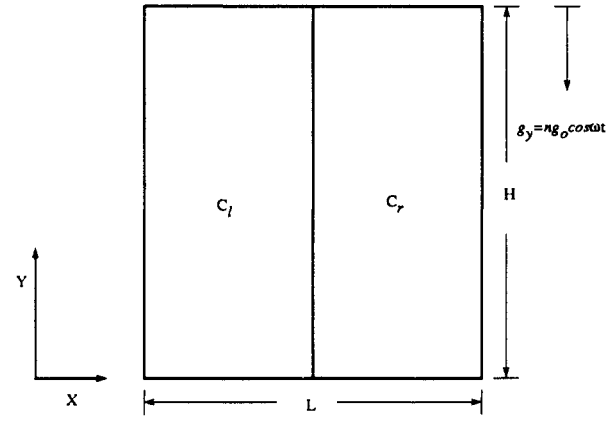

Fig. 1 Physical description of two fluids in contact at an interface. The heavy and light fluid occupy the left and right regions, respectively.

where

$$\frac{Gr}{Re^2}=\frac{\Delta\rho}{\bar{\rho}}\frac{ng_o}{\omega^2 H} \tag{11a}$$

$$Re=\frac{\omega H^2}{\bar{\nu}} \tag{11b}$$

$$Pe_D=\frac{\omega H^2}{\tilde{D}_{lr}} \tag{11c}$$

$$A\!R=\frac{H}{L} \tag{11d}$$

In the preceding set of dimensionless equations, since we have a nonhomogeneous media, a vorticity creation term arises. Four significant large scale parameters result from the nondimensionalization. Various length scales also occur in the problem. In addition to the large geometric length scales H and L, there are also two small boundary-layer length scales, $\delta_s \equiv \sqrt{\bar{\nu}/\omega}$, based on the Stokes length scale,[16] and $\delta_D \equiv \sqrt{\tilde{D}_{lr}/\omega}$. These diffusion length scales can be used to classify the response of the interface evolution to external acceleration forcing. If we replace the geometric length scales by the diffusive length scale δ_s in the dimensionless set of equations, then the number of parameters reduces to two, namely:

$$Pe_D=\frac{\bar{\nu}}{\tilde{D}_{lr}} \tag{12a}$$

$$\frac{Gr}{Re^2}=\frac{\Delta\rho}{\bar{\rho}}\frac{ng_o}{\omega^{3/2}\bar{\nu}^{1/2}} \tag{12b}$$

where $Pe_D = Sc$, the Schmidt number, and $Re_s \equiv Gr/Re^2$ denotes the Stokes-Reynolds number. The Stokes-Reynolds number represents the relative importance of buoyancy to inertia forces; it is also a measure of the importance of nonlinear effects from the point of view of the large scale computations. Even if nonlinearity is unimportant on the large scale, it may be of great importance in interface evolution on the small scale. As shown by Jacqmin and Duval,[17] small-scale Kelvin-Helmholtz and Rayleigh-Taylor instabilities can be generated at the interface. These are not necessarily resolved by the larger scale computations of this paper. However, a good measure for predicting the evolution of the interface leading to chaotic mixing can be expressed in terms of the Stokes-Reynolds number, in which the small length scale is employed. Because we are interested in interface evolution, δ_s is more appropriate than δ_D for scaling. For long time solutions, not discussed in this paper, in which the flowfield becomes stratified, δ_D would be more appropriate. In this case, the problem reduces to one significant parameter, namely, $Re_D = Re_s\sqrt{Sc}$.

Solution Technique

The previous set of equations is solved by a finite-difference technique. The flow is initialized as motionless, with the preceding indicated initial values of concentrations. The oscillating acceleration field coupled to the density jump at the interface then forces convection. The numerical solution at each time step is carried out by sequentially solving first the vorticity equation, then the steam function equation, and lastly the concentration equation. The nonlinear terms in the vorticity and concentration equations are discretized in time using the explicit third-order Adams-Bashforth scheme. Diffusive and stream function terms are discretized spatially by central differencing. The concentration equation advective terms are calculated using a number of techniques, among them central differencing, upwind differencing, and the flux corrected transport (FCT) method of Boris and Book.[18] The FCT method, used for the numerical studies, yields results on about the same level of accuracy as central differencing while eliminating false oscillations and minimizing numerical diffusion. This method is specially suited for sharp density difference cases because of its ability to handle discontinuities such as shocks and steep gradients. The technique is mass conserving, stable, and, in our case, assures positivity of the concentration field in order to eliminate false oscillations. For the vorticity boundary condition, we used the second-order Woods formula,[19] namely,

$$\zeta_w=\frac{3(\Psi_{w+1}-\Psi_w)}{(\Delta q)^2}-\frac{1}{2}\zeta_{w+1}+O(\Delta_q^2) \tag{13}$$

This boundary condition is derived from a Taylor series expansion of the stream function from the wall. In addition to being second-order accurate, we found it to be stable for our computations.

Discussion and Numerical Results

Parametric Range

Inside the Space Shuttle environment, the g-jitter frequency, $\omega/2\pi$, ranges from 0.1 to 10 Hz, whereas its amplitude, ng_o varies from $10^{-3}g_o$ to $10^{-5}g_o$[2]. The space experiments of Radcliffe et al.[6] investigated the mixing of chloroform and heptane (large density difference), as well as pure methanol and methanol solutions with yellow or blue dye (small density difference) by counter-diffusion inside an enclosure under g-jitter microgravity conditions. We use these two sets of fluids in our computational examples to cover a large range of possible density differences. For the large density difference fluids, the properties are $\bar{\nu}=0.00495$ cm^2/s,[20] $\Delta\rho/\bar{\rho}=0.721$, and $\tilde{D}_{lr}=2\times10^{-5}$cm^2/s. With these liquid properties and for the specific case where $\omega=2\pi/3$ s^{-1}, and $ng_o=10^{-3}_{g_o}$, our dimensionless parameters become $Gr/Re^2=0.0165$, $Re=4.24\times10^4$, $Re_s=3.41$, $Sc=247$, and $Pe_D=1.05\times10^7$. Whereas, for the low density difference fluids, the properties are taken to be $\bar{\nu}=0.00702$ cm^2/s,[9] $\Delta\rho/\bar{\rho}=0.00215$, and $\tilde{D}_{lr}=0.87\times10^{-5}$ cm^2. Cavity sizes (see Fig. 1) for which we will present calculations cover the following range: H and L = 10, 5, 2, 1, and 0.6 cm for the square cavity. Variations for the horizontal cavity, keeping $L=10$ cm, include H = 5, 2, 1, and 0.5 cm. Similar variations in size for the vertical cavity are obtained by reversing the values of L and H. Our parametric studies cover the following range of parameters: $A\!R=0.05$-20, $Gr/Re^2=9.61\times10^{-6}$-0.5887, $Re=1.06\times10^2$-4.24×10^4, $Re_s=8.30\times10^{-4}$-14.86, $Sc=241$, and 807, and $Pe_D=3.78\times10^4$-1.04×10^8.

Square Cavity

We next present calculations for the square cavity. We show that the interface evolution consists of deformation and oscillation. Deformation of the interface occurs for low values of Gr/Re^2, and at those low values the interface does not necessarily oscillate. However, oscillation of the interface is always accompanied by deformation for certain ranges of Gr/Re^2. In the first series of studies, we consider effect of grid size, details of interface evolution, and effect of decreased cavity size. The parametric ranges are show in Table 1 with corresponding Figs. 2-5. In Fig. 2, we show the effect of grid size on resolution of the details of an interface for both the maximum cavity size and time considered. Whereas the 36×36 grid size predicts the correct trend, the 54×54 grid picks up the finer details. Doubling the grid size to 72×72 enhances the finer details. These trends indicate that for our computations the 72×72 grid size gives adequate large scale resolution of the interface region. However, we found that for certain cavity sizes the 36×36 grid size gives equivalent results to the 72×72 grid in predicting interfacial configuration. Unless noted, all parametric studies are done using the 72×72 grid size.

Table 1 Parametric range for the square cavity

Case	Figure	$\mathcal{R}$	Re_S	Gr/Re^2	Re	Pe_D
1	3a,3b	1	3.41	0.0166	4.24×10^4	1.05×10^7
2	5a	1	3.41	0.0331	1.06×10^4	2.62×10^6
3	5b	1	3.41	0.0828	1698	4.19×10^5
4	5c	1	3.41	0.1656	424	1.05×10^5
5	5d	1	3.41	0.2759	153	3.78×10^4

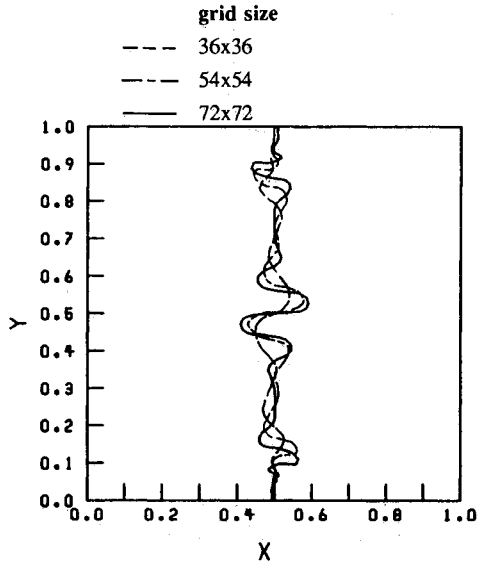

Fig. 2 Effect of grid size.

Interface Deformation

We now consider details of interface evolution showing deformation of the interface for the first 10 cycles of oscillation. These calculations are for the 10×10 cm cavity. We show the first cycle of oscillation, in Fig. 3a, and subsequent cycles in Fig. 3b. Nine concentration contour lines are shown at the interface region in increments of 0.1. In response to the g-jitter initially pointing downward, within the first quarter cycle ($\tau=1/4$) the heavier fluid on the left side of the cavity flows down and the lighter fluid flows up. The g-jitter vector, which was initially downward, changes direction. A clockwise rotating flow results from the hydrostatic pressure imbalance, which deforms the interface at the top and bottom of the cavity. There is a near discontinuity of tangential velocity. This characteristic of the flow is emphasized by the sharp corner effects shown in the stream function plots. Thus, the interface behaves like a vortex sheet. This portion of the cycle results in the most intense flow. The enclosure geometry forces a flow that begins to rotate. However, at the second quarter cycle ($\tau=1/2$) the flow changes direction. The g-jitter vector,which had changed direction, goes through a relative minimum. The rotation is halted when the flowfield changes direction; then vorticity begins to be eliminated. The interface does not return to its original position and displays a phase lag. A residual shear layer flow forms in the neighborhood of the interface caused by vorticity production in the earlier part. If the interface was frozen in position, despite motion of the fluid, the net integrated vorticity production from π to τ would be exactly zero and the flow at π or $\tau=1/2$ would be motionless. Because the interface distorts and moves, there remains a net vorticity in the fluid that drives a local shear flow in the vicinity of the interface. The vorticity is like a dipole layer, so both velocity shear and velocity itself are found only near the interface. The flow reaches its maximum strength at the third quarter cycle ($\tau=3/4$), where it is again rotating in the counterclockwise sense. The total force from the potential energy of the flow pushes against the interface in the opposite sense as

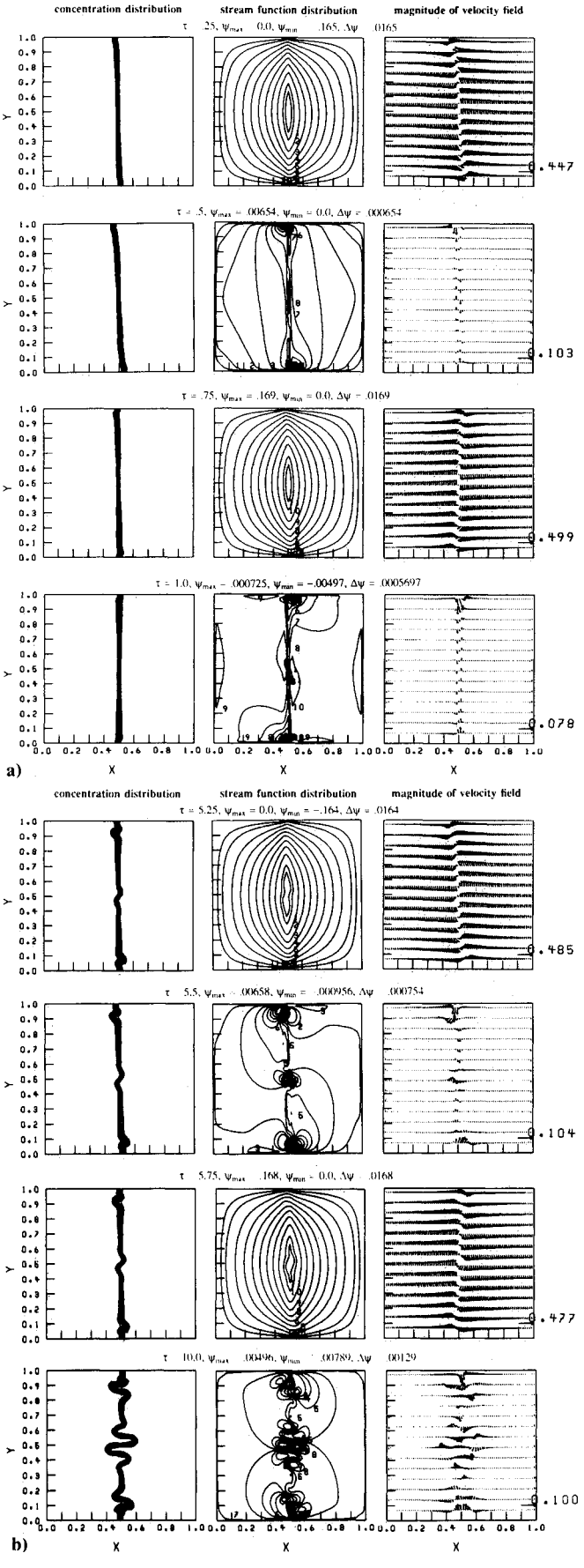

Fig. 3 Evolution of the interface and kinematics of the flowfield. (The minimum and maximum values of the stream function correspond, respectively, to Ψ_{min} and Ψ_{max} with increments of $\Delta\Psi$. They are divided into 10 intervals varying from Ψ_1 to Ψ_{11}). The number on the bottom right-hand side of the vector fields represents the relative scaling of the vectors.

that of the first quarter cycle. As motion proceeds to the fourth quarter cycle ($\tau = 1$), a relative maximum of the forcing function is reached and the flow changes direction, displaying a residual shear flow in the opposite sense as that of the second quarter cycle. An increase in both vorticity generation at the walls and the interface results. This oscillation in flowfield continues for each period as time increases, and its effect is deformation of the interface. Thus, for increasing time within a cycle, the flowfield alternates sinusoidally between a rotating clockwise and counterclockwise flow when the g-jitter vector changes direction, and transforms to a residual shear flow when the g-jitter vector goes through a relative minimum or maximum.

Subsequent deformation of the interface due to the flowfield is shown in Fig. 3b. In addition to the deformation of the interface near the top and bottom of the cavity, which was apparent for short times, deformation of the center of the interface becomes more prominant at the fifth quarter cycle ($\tau = 5.25$). This occurs because of the net effect of the rotating and residual shear component of the flow on the interface structure. Unlike the early part of the first cycle, the flowfield induces a kink at the center of the interface where it has its maximum strength. When the g-jitter vector goes through a relative minimum, in addition to the residual shear flow, vortex generation at the center of the interface and ends of the cavity results. These net effects cause deformation of the center of the interface, and these deformations amplify for increasing time. The fifth half ($\tau = 5.5$) and fifth three quarter ($\tau = 5.75$) cycles are similar to the first half ($\tau = 0.5$) and first three quarter cycles ($\tau = 0.75$) in terms of trends. However, vortex generation at the interface increases. Finally, after five more cycles ($\tau = 10$), generation of vortex at the interface is intensified, and a wavy interfacial structure with larger amplitudes results. The vortices along the interface form two distinct rows similar to a vortex street.

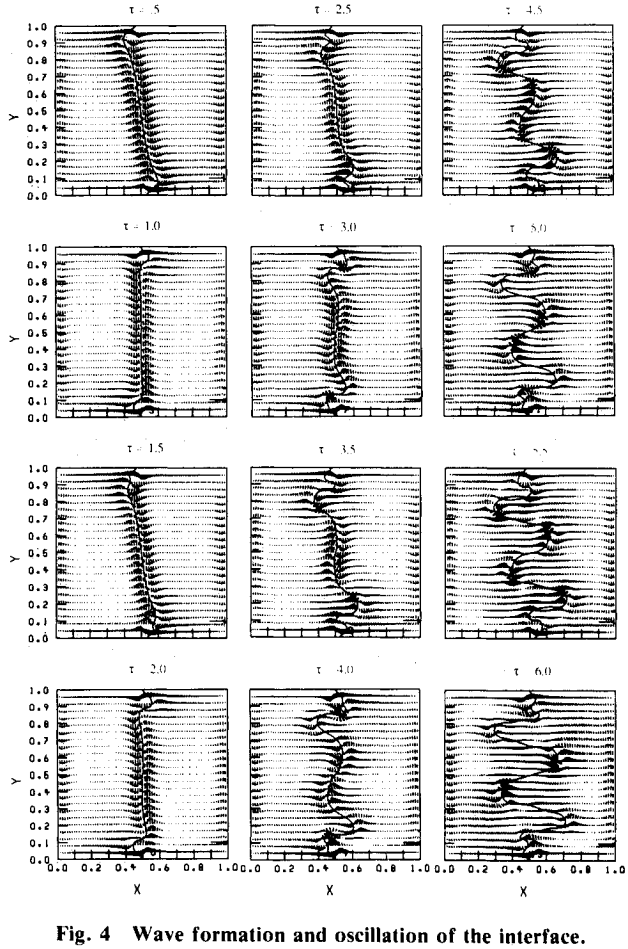

Fig. 4 Wave formation and oscillation of the interface.

Wave Formation and Oscillation of the Interface

Even though the initial deformation of the interface is illustrated in Fig. 3, its oscillation is not readily apparent, since Gr/Re^2 ($=0.0166$) is low. In Fig. 4, we show case 3 in Table 1. This shows both oscillation and deformation of the interface leading to wave formation for the first six oscillations in increments of one-half cycle. For clarity, only the contour line $C = 0.5$ is shown. The figure shows the flowfield at the minimum and maximum of the forcing function, which also corresponds to the minimum and maximum of the g-jitter vector. As we pointed out earlier, when the g-jitter vector goes through a relative minimum or maximum, the flowfield transforms to a residual shear flow. In this case, the residual shear flow is intensified. As the flow evolves, the number of vortices generated at the interface increases. These flow configurations are similar to the vortex sheet evolution associated with Kelvin-Helmholtz instability waves. Unlike most classical analysis of shear flow problems, we have an oscillating flow that behaves alternately with rotating and residual shear during a cycle. During the first half cycle, the interface is shifted to the left, and at the full cycle, it is almost restored to its original position. Boundary-layer formation at the interface and side walls also result. The second and subsequent oscillations occur similarly. In this case, for large Gr/Re^2 ($=0.0828$), the net effect of the rotating and residual shear causes both deformation and oscillation of the interface. This type of behavior is similar to problems associated with discrete vortex approximation to investigate short time evolution of a vortex sheet,[12-14] and long time vortex sheet evolution past the critical time.[15] Though our flow is more complex than most classical analysis of vortex sheet and Kelvin-Helmholtz instability, it demonstrates the evolution of a vortex production sheet inside a rectangular cavity due to an oscillated flowfield when viscous effects and interfacial mass diffusion are also taken into account.

Effects of Cavity Size

Effects of cavity size on the dynamics of the interface shape and its relationship to the dimensionless parameters and set of field equations are now investigated. Because $AR = 1$, both horizontal and vertical spatial dependence in these equations are of equal importance. The parametric range is shown in Table 1, cases 2-5, and corresponding Figs. 5a-5d, for a fixed oscillation time $\tau = 10$. According to the dimensionless set of equations, the parameters Re and Pe_D are proportional to H^2, whereas Gr/Re^2 is proportional to $1/H$. Therefore, as the cavity size decreases, there is faster change in Re and Pe_D, which means that the flow becomes effectively more viscous. From the dimensionless set of field equations, these parametric ranges indicate that the nonlinear convective terms in the vorticity equation are dominant, but the viscous diffusion terms become important for a low Reynolds number. The cases when viscous effects become progressivly important are shown in Figs. 5a-5d. These cases are in contrast to Fig. 3, $1/Re \ll Gr/Re^2$, where the flow was basically inviscid and the interface between the two fluids deformed while remaining sharp. In Fig. 5a, larger amplitude waves are formed and an increase in size of the vortices also results. These vortices are in proportion to the curvature and the number of waves at the interface; they form two rows on either side of the interface and propagate in the flowfield, depending on the amplitude. Further decrease in the size of the cavity results in a decrease in the number of waves formed at the interface and also the number of vortices generated. However, larger amplitude waves are formed and the interface also oscillates, as shown in Fig. 4. These oscillations and generation of vortices at the interface can serve as a mechanism to enhance mass transport. This becomes more apparent in Fig. 5c, where there is a transition from multiple waves to single wave formation with a relatively larger vortex size. For this cavity size (1×1cm), diffusion of mass at the interface has become important. In addition, the boundary layer at the side walls increased in relative

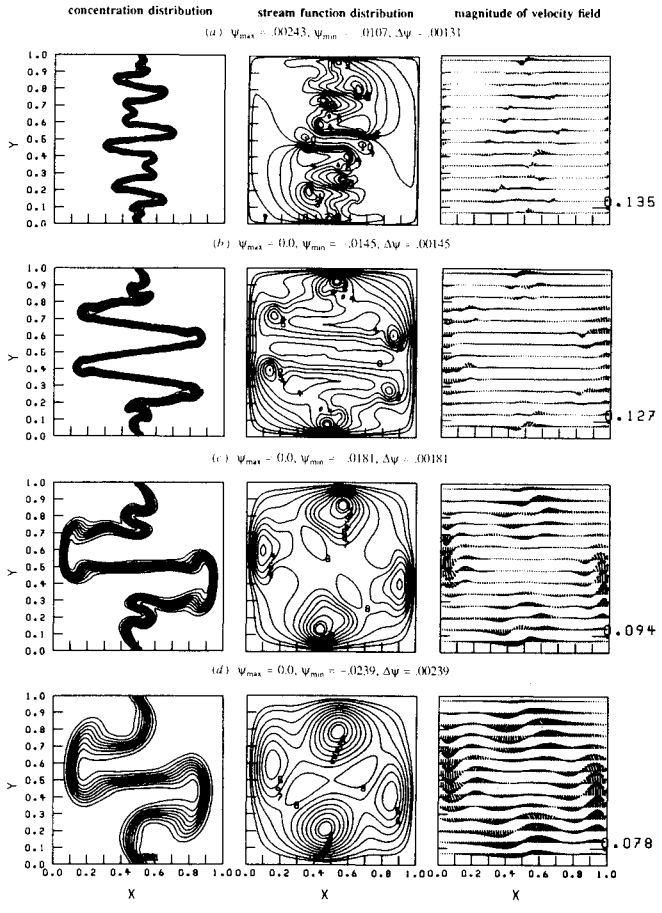

Fig. 5 Configuration of the interface and flowfield for decreasing cavity size at $\tau = 10$.

thickness and amalgamates with the entire flowfield. The combination of increased amplitude oscillation and larger vortex size rotating in the flowfield promotes a mechanism for mass transport, as shown in Fig. 5d. In this case the cavity is so small (0.6 × 0.6 cm) that mass diffusion is indeed an important component of overall mass transport. The mass transport is localized to the interface region and is shown by the diffusion of the concentration field into the flow. These parametric variations indicate that the amplitude of wave formation is governed essentially by the magnitude of the nonlinear convective terms, Gr/Re^2. Even though the concentration field equation indicates that the convective transport is dominant over mass diffusion, interface oscillation and vortices rotating in the flowfield can provide the mechanism for localized mass transport at the interface.

Horizontal Narrow Cavity

The parametric studies where $A = 1$ permitted us to study the evolution of the interface when both horizontal and vertical spatial dependence is of equal importance. We now consider the horizontal narrow cavity in which H decreases (see Fig. 1). Table 2 displays the range of parameters covered for this case. From the dimensionless set of equations, it can be seen that as A decreases, the spatial dependence in the horizontal direction becomes of secondary importance in comparison to the vertical direction, and the vorticity production term also becomes less important. Cases 6-8 in Table 2 correspond to cases 2-4 in Table 1, except for the change in A. Figures 6a-6c show the resulting evolution of the flowfield at $\tau = 10$. In comparison to Figs. 5a-5c (cases 2-4), in which the cavity height is equivalent to those in Figs. 6a-6c, the amplitude of the interface and the number of vortices in the flow decreased. This results because the horizontal dependence in the dimensionless field equations, which gives rise to the amplitude size

Table 2 Parametric range for the horizontal narrow cavity

Case	Figure	A	Re_s	Gr/Re^2	Re	Pe_D
6	6a	0.50	3.41	0.0331	1.06×10^4	2.62×10^6
7	6b	0.20	3.41	0.0828	1698	4.15×10^5
8	6c	0.10	3.41	0.1656	424	1.05×10^5
9	6d	0.05	3.41	0.3312	106	2.62×10^4

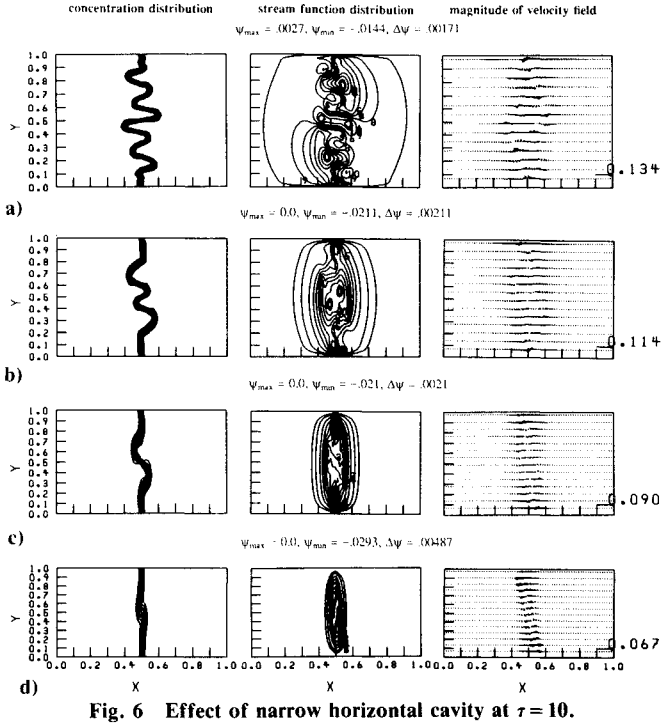

Fig. 6 Effect of narrow horizontal cavity at $\tau = 10$.

of the interfacial wave, becomes much smaller than the vertical dependence. Hence a reduction of wave amplitude results. At the same time, since A multiplies the vorticity production term, the number of vortices generated at the interface also decreases. Thus, for low narrow horizontal cavities, the flow is restricted to the interface region and decays outside that region where it becomes nearly quiescent. Even though the magnitude of Gr/Re^2 increases for a horizontal narrow cavity, the amplitude of the waves decreases, which is contrary to the cases for $A = 1$. This happens because A becomes the dominant parameter, and its effect on interface evolution becomes readily apparent by inspecting the field equations. However, similar to Fig. 5a, in Fig. 6a a stacking phenomena occurs in which vortex rows on both sides of the interface form. Decreasing the cavity size results in the formation of a flowfield with a small core flow embedded in a larger one [Fig. 6d (five streamlines are shown)], and very slight deformation of the interface. The flow also becomes viscously dominated, and vortices diffuse toward the center of the cavity.

Vertical Narrow Cavity

We now consider the other end of the spectrum, in which the length of the cavity is decreased in order to approach a narrow vertical slot. The corresponding parametric variations are shown in Table 3 and illustrated in Fig. 7a-7d for $\tau = 10$. Cases 10-13 are analogous to case 1; they have the same cavity height as Fig. 3 except for changes in length. According to the set of field equations and the magnitude of the parameters, the vertical component of the velocity becomes dominant over the horizontal component. This means that the production of vorticity should increase at the interface and larger amplitude waves should also result, in contrast to the horizontal narrow cavity. Such trends are shown in Fig. 7, with important differences. Comparison of Fig. 7a to Fig. 3 ($\tau = 10$) shows equivalent wave amplitude near the center of the cavity, and an

increase in both amplitude and number of waves near the top and bottom of the cavity. This increase near the ends of the cavity is expected. (Recall that the hydrostatic pressure field gives rise to the flow and subsequent deformation of the interface occurs near the ends of the cavity.) With a decrease in width of the cavity, the equivalent hydrostatic pressure field is more effective at establishing intensive flowfields that generates vorticity, and gives rise to larger amplitude waves near the top and bottom of the cavity. Similar to Fig. 6a, a stacking phenomena (see Fig. 7a) is formed with rows of vortices on both sides of the interface. As the cavity is made narrower, (Fig. 7b) the vertical component of the velocity becomes dominant and gives rise to an intensive core shear flow near the center of the cavity. This shear flow then suppresses wave formation at the core region. The structure of both the interface and flowfields is transformed to one where the core region increases as the aspect ratio increases. The interfacial wave amplitude also increases near the ends of the cavity until viscous action becomes overwhelming. These trends are shown in subsequent figures (Figs. 7b–7d). In the limiting case of the very small narrow cavity (Fig. 7d), the boundary layers at the walls amalgamate with the core shear flow and become an effective mechanism for promoting local mass transport at the interface.

Effects of Forcing Function

Amplitude Variation

For the preceding parametric variations, the relative importance of the linear viscous diffusion and the nonlinear convective terms cannot be addressed independently, since they are both dependent on the variation of the geometric length scales of the cavity. Keeping the geometrical length scales fixed, we can vary the g-jitter amplitude. The amplitude variation affects only the magnitude of Gr/Re^2 based on the large length scale and Re_s based on the small length scale, while all other parameters remain fixed. This allows for independent variation of the nonlinear convective terms. The parametric ranges for g-jitter amplitude variation, which shows effects of the nonlinear convective terms, are shown in Table 4. As the nonlinear terms become important, their effect is clearly to increase the amplitude and the number of waves formed at the interface, as shown in Fig. 8. For this parametric range, computed using 36×36 grid size, higher grid size did not have any significant effect on the interface structure.

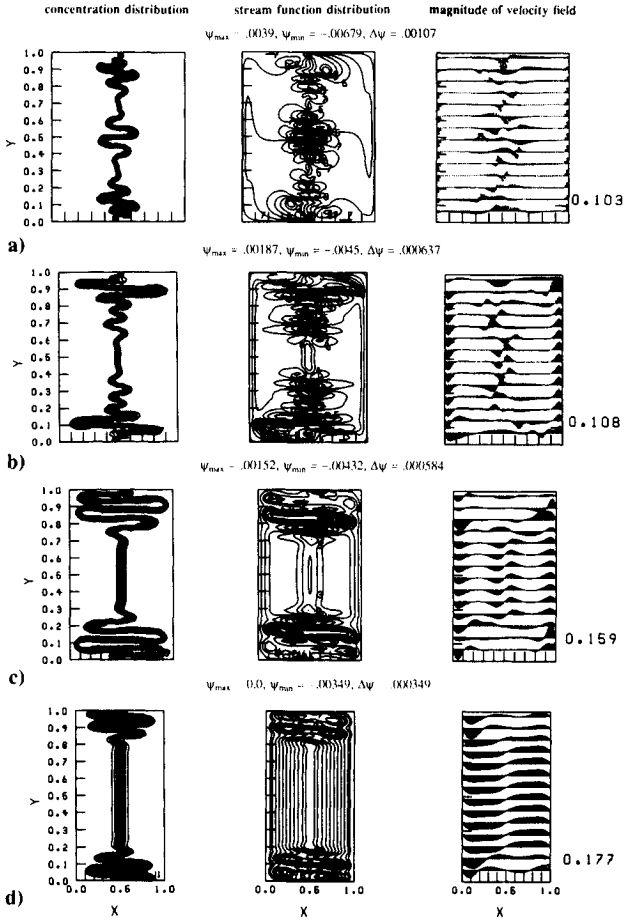

Fig. 7 Effect of narrow vertical cavity at $\tau = 10$.

Frequency Variation

The g-jitter amplitude variation allowed for a first glimpse at the relationship between the large scale phenomena measured by Gr/Re^2 and the small scale phenomena measured by Re_s. The parameter Re_s may also be interpreted as the ratio of frequencies, that is, the frequency response of the interface region $(\Delta\rho/\bar{\rho} \cdot ng_o/\bar{\nu}^{1/2})$ to the input frequency ω of the gravitational flield. Thus, as the input frequency is varied, one can find near resonance conditions. In this parametric variation (see Table 5), we show the effect of the small scale on the interface evolution by varying the g-jitter frequency. The large scale parameters are also shown in Table 5, for comparison purposes with previous calculations. As we have mentioned, for the small scale interpretation of the results, the dimensionless field equations become dependent on two parameters only, Re_s and Sc. Thus, the magnitude of the nonlinear convective terms for both vorticity and concentration is dependent only on Re_s, and the mass diffusion terms depend on Sc. According to these equations, since Re_s is directly proportional to $\omega^{3/2}$, we would expect a rapid growth in the amplitude of the interface as ω increases. Such trends are shown in Figs. 9 and 10. In Fig. 9a, we consider a limiting case, very small Re_s, corresponding to the small density difference experiments of Radcliffe et al.[6] The result shows that at $\tau = 10$ oscillations the

Table 3 Parametric range for the vertical narrow cavity

Case	Figure	A	Re_s	Gr/Re^2	Re	Pe_D
10	7a	2	3.41	0.0166	4.24×10^4	1.05×10^7
11	7b	5	3.41	0.0166	4.24×10^4	1.05×10^7
12	7c	10	3.41	0.0166	4.24×10^4	1.05×10^7
13	7d	20	3.41	0.0166	4.24×10^4	1.05×10^7

Table 4 Parametric range for g-jitter amplitude variation

Case	Figure	A	Re_s	Gr/Re^2	Re	Pe_D
14	8	1.29	1.6	0.0973	264	1.06×10^5
15	8	1.29	3.2	0.1946	264	1.06×10^5
16	8	1.29	4.7	0.2919	264	1.06×10^5

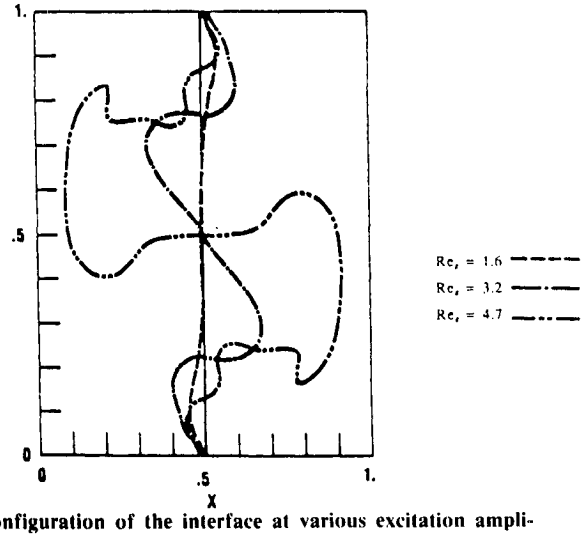

Fig. 8 Configuration of the interface at various excitation amplitudes, $C = 0.5$ and $\tau = 4$.

Table 5 Parametric range for g-jitter frequency variation

Case	Figure	$\mathcal{R}$	Re_s	Sc	Gr/Re^2	Re	Pe_D
17	9a	1	8.30×10^{-4}	807	9.61×10^{-6}	7459	6.02×10^{6}
18	9b	1	5.25	247	0.1472	1273	3.14×10^{5}
19	9c	1	5.25	247	0.1472	1273	3.14×10^{5}
20	9d	1	9.67	247	0.3312	849	2.09×10^{5}
21	10	1	14.86	247	0.5888	637	1.57×10^{5}

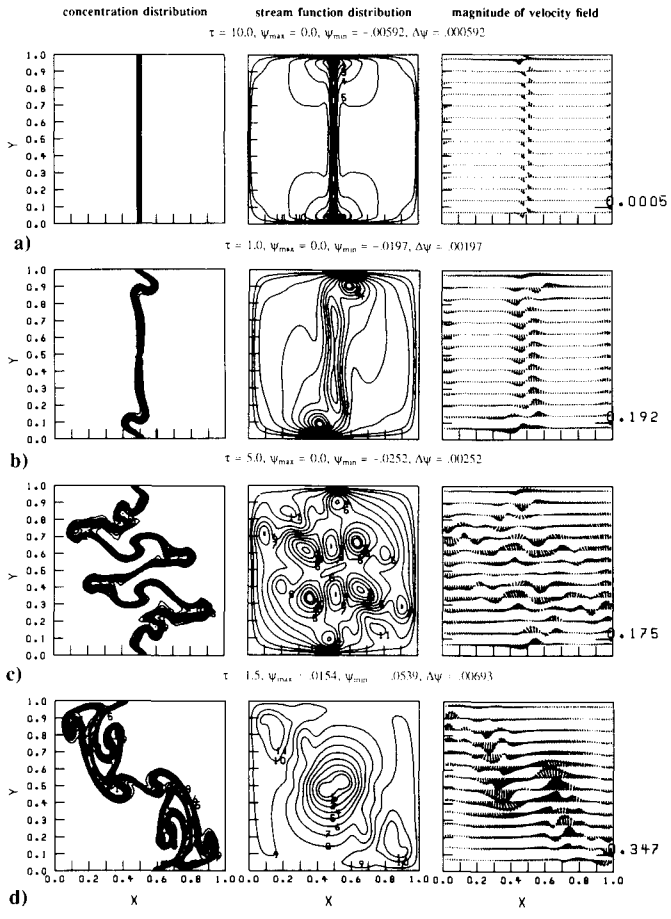

Fig. 9 Stabilized and destabilized interfaces, and transition to incipient destability.

interface is stable against Kelvin-Helmholtz instability, and remains sharp and undeformed. For this case, mixing of the fluids would ultimately occur by mass diffusion over a long time scale, which is in agreement with the experimental trends of Radcliffe et al.[6] The interface evolution leading to incipient destability, near resonant conditions, is shown in Figs. 9b and 9c. Unlike the preceding cases, which result in a stable interfacial wave structure, in Fig. 9b at $\tau=1$ the formation of an unstable break wave is shown. This break wave oscillates and grows with time, and at $\tau=5$ the interface is transformed to an incipient destability situation that ultimately results in the breakdown of the interface. This is accomplished by an increase in the number of vortices in the flow. Thus, $Re_s=5.25$ represents an approximate value where chaotic instability is about to occur. In this case, oscillation of the interface also occurs. An increase in Re_s (Fig. 9d) results in a continuous deformation of the interface without any oscillations, unlike the preceding case, leading to a complex break wave pattern. The interfacial structure displaying incipient destability occurs for a shorter time, $\tau=1.5$.

In Figs. 9c and 9d, we showed the interface structure at incipient destability near and beyond the critical Stokes-Reynolds number. The evolution of interfacial structure illustrating chaotic mixing is shown in Fig. 10. This case shows the resulting interfacial structure when the g-jitter frequency is well within the resonance range. We show the details of the first one and a half cycles, and the resulting configuration at the tenth oscillation. Comparison to Fig. 9 at the respective time shows that larger amplitude deformations result. During the first cycle of oscillation (see Fig. 10), the interface is unstable against Rayleigh-Taylor instability in the interim to chaotic mixing. Similar interfacial features for the classical Rayleigh-Taylor instability are discussed by Tryggvason.[21] The continual deformation of the interface leads to a double-branched vortex and also exhibits vortex sheet rollup[14] during the first cycle. Interfacial breakup soon follows at $\tau=1.5$. The interface evolves into a random structure indicating chaotic mixing, $\tau=10$. In the accompanying flowfield, a large number of rotating vortices are also generated. These vortices serve as a stirring mechanism to promote mixing. These computations also show that near the critical Re_s, the phenomena leading to interface breakup is governed by the small length scale. Cases 3-5 bracket case 19 in terms of the large scale parameter Gr/Re^2, yet incipient destability of the interface did not occur for these cases. This reinforces the fact that the small-scale phenomena indicated by the Stokes-Reynolds number is a good predictor of chaotic mixing.

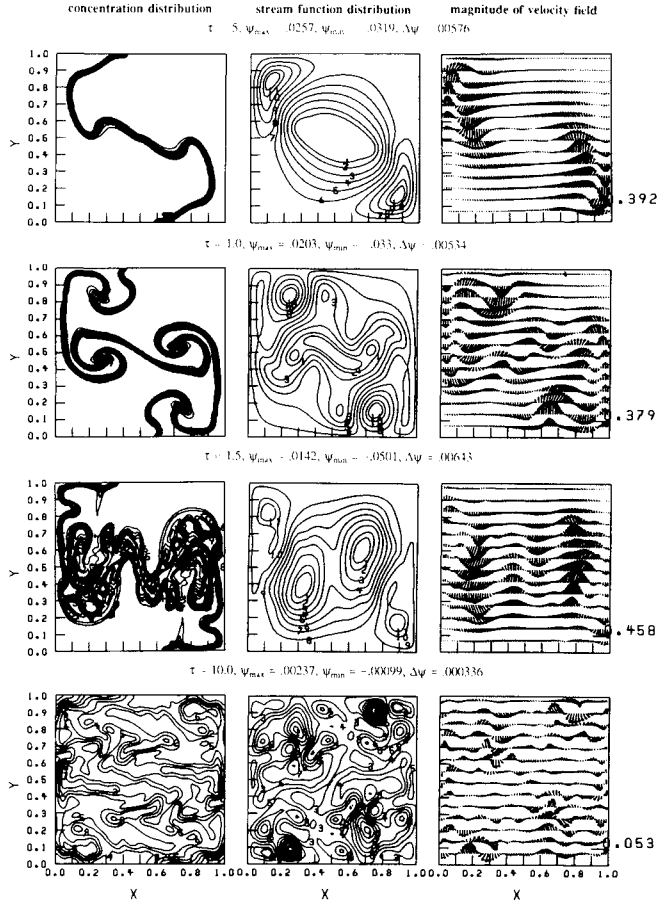

Fig. 10 Transition of the interface to random structure, indicating chaotic mixing.

Conclusions

Interfacial dynamics of two fluids subjected to g-jitter have been studied to predict motion of the interface and kinematics of the flowfield for a wide range of parameters. The interface evolves like a vortex source sheet. The characteristics of interface evolution are governed by two length scales: a large length scale based on the geometry of the cavity, in which the field

equations become dependent on four parameters, namely, $\mathcal{R}$, Gr/Re^2, Re, and Pe_D, and a small Stokes length scale, which is independent of geometry and reduces the parametric dependence of the field equations to two parameters, Re_s and Sc. The applicable scale depends on a criterion based on a critical magnitude of Re_s for incipient destability, which is approximately 5.25. For flows below the critical value of Re_s inside a square cavity, interfacial deformation depends mainly on the magnitude of Gr/Re^2. The interface is stable against Kelvin-Helmholtz instability for very low values of Gr/Re^2 ($Gr/Re^2 = 9.61 \times 10^{-6}$). For values of $Gr/Re^2 = 0.017$ and higher, the interface becomes unstable against Kelvin-Helmholtz instability and deforms into wavy structures. These interfacial deformations oscillate as time increases for Gr/Re^2 on the order of 0.03 or higher. Vortices are produced at the interface and, for interfacial structures with a large number of waves, these vortices form stacking rows on both sides of the interface. We show that vortices along the interface can serve as a stirring mechanism to promote mass transport at the interface. For the horizontal cavity, we show that both the number and amplitude of waves decrease as the size of the cavity decreases, and a weak flow results with inner and outer core at the interface whereas, for the narrow vertical cavity an intense core shear flow develops that amalgamates with the boundary layer at the walls and also gives rise to local mass diffusion at the interface.

Near the critical Stokes-Reynolds number, the interface is destabilized and breakup of the interface into distinct concentration pockets follows. The amplitude of the interface grows rapidly with time and oscillates. Unlike the cases below the critical value, the waves formed at the interface take the form of unstable breaker waves. Beyond the critical value, no oscillation of the interface occurs. Instead, it deforms continuously into complex breaker wave patterns and exhibits Rayleigh-Taylor morphology with distinctive features of double-vortex formation and vortex rollup. Once the interface breaks, chaotic mixing follows, with a random distribution of concentration pockets in the cavity. The flowfield also has a large number of vortices, which serves as a vigorous stirring mechanism to promote mixing.

For practical crystal growth applications under microgravity environment, the above work delineates parametric conditions for which g-jitter can be effective in driving convective flow fields. These flow fields can be significant enough to cause unwanted convection during experiments. In particular, even in the solution crystal growth techniques which are designed to take advantage of the low gravity conditions, significant levels of convection can be generated. Therefore, precautionary measures, such as vibration isolation tables, should be considered for solution crystal growth experiments in which minimal levels of convection are desired.

Acknowledgments

We gratefully acknowledge R. K. Crouch and M. C. Lee, Code SN Microgravity and Applications Research, for supporting our work. Comments from the reviewers and the many discussions with M. Kassemi were very helpful. We thank T. K. Glasgow, Branch Chief of Processing and Technology in the Materials Division at NASA Lewis, for his support.

References

[1]Spradley, L. W., Bourgeois, S. W., and Lin, F. N., "Space Processing Convection Evaluation, *G*-Jitter Convection of Fluids in Low Gravity," *Proceedings of the AIAA 10th Thermophysics Conference*, New York, May 1975, pp. 675-695.

[2]Kamatoni, Y., Prasad, A., and Ostrach, S., "Thermal Convection in the Enclosure Due to Vibrations Aboard Spacecraft," *AIAA Journal*, Vol. 19, No. 4, 1981, pp. 511-516.

[3]Galster, G., and Nielsen, K. F., " Crystal Growth From Solution," *Proceedings of the 5th European Symposium on Materials Sciences under Microgravity*, Schloss Elmau, West Germany, Nov. 1984, pp. 189-191.

[4]Gerbi, D. J., Egber, W. C., Ender, D. A., Leung, P. C. W., Rochford, K. B., Virden, J. W., and Cook, E. L., "Growth of Organic Crystals in a Microgravity Environment," *Journal of Crystal Growth,* Vol. 76, July 1986, pp. 673-680.

[5]Robert, M. C., Lefaucheux, F., and Authier, A., "Growth and Characterization of Brushite and Lead Monetite—Simulation and Results," *Proceedings of the 5th European Symposium on Materials Sciences under Microgravity*, Schloss Elmau, West Germany, Nov. 1984, pp. 193-199.

[6]Radcliffe, M. D., Steffen, J. E., Cook, E. L., Cutting, J. F., Miller, L. R., Drake, M. C., Schroeder, F. S., and Stevens, Jr., "Organic Crystals in Low Earth Orbit," *Journal of Crystal Growth*, Vol. 92, Oct. 1988, pp. 581-590.

[7]Sanni, S. A., Fell, C. J. D., and Hutchison, P., "Diffusion Coefficients and Densities for Binary Organic Liquid Mixtures," *Journal of Chemical and Engineering Data*, Vol. 16, No. 4, 1971, pp. 424-427.

[8]Sanni, S. A., and Hutchison, P., "Diffusivities and Densities for Binary Liquid Mixtures," *Journal of Chemical and Engineering Data*, Vol. 18, No. 3, 1973, pp. 317-322.

[9]Wei, I-C, and Rowley, R. L., "Binary Liquid Mixture Viscosities and Densities," *Journal of Chemical and Engineering Data*, Vol. 29, 1984, pp. 232-335.

[10]Chandrasekhar, S., *Hydrodynamic and Hydromagnetic Stability*, Oxford University Press, Oxford, UK, 1961, pp. 481 598.

[11]Patnaik, P. C., Sherman, F. S., and Corcos, G. M., "A Numerical Simulation of Kelvin-Helmholtz Waves of Finite Amplitude," *Journal of Fluid Mechanics*, Vol. 73, Part 2, Jan. 1976, pp. 215-240.

[12]Rosenhead, L., "The Formation of Vortices from a Surface of Discontinuity," *Proceedings of the Royal Society,* Harrison and Sons, London, Vol. 134, Jan. 1932, pp. 170-192.

[13]Zalosh, R. G., "Discretized Simulation of Vortex Sheet Evolution with Buoyancy and Surface Tension Effects," *AIAA Journal*, Vol. 14, No. 11, 1976, pp. 1517-1523.

[14]Rottman, J. W., and Olfe, D. B., "Comment on 'Discretized Simulation of Vortex Sheet Evolution with Buoyancy and Surface Tension Effects,'" *AIAA Journal*, Vol. 15, No. 8, 1976, pp. 1214-1215.

[15]Krazny, R., "Desingularization of Periodic Vortex Roll-up," *Journal of Computational Physics*, Vol. 65, July 1986, pp. 292-313.

[16]Schlichting, H., *Boundary Layer Theory*, 7th ed., McGraw-Hill, New York, 1979, pp. 90-95.

[17]Jacqmin, D., and Duval, W. M. B., "Small Scale Instabilities Caused by Oscillations Normal to a Viscous Fluid-Fluid Interface," *Journal of Fluid Mechanics*, Vol. 196, Nov. 1988, pp. 495-511.

[18]Boris, J. P., and Book, D. L., "Flux-Corrected Transport I: SHASTA—A Fluid Transport Algorithm That Works," *Journal of Computational Physics*, Vol. 11, Jan. 1973, pp. 38-69.

[19]Roache, P. J., *Computational Fluid Dynamics*, Hermosa, Alburquerque, NM, 1972, pp. 139-174.

[20]Weast, R. C., Astle, M. J., and Beyer, W. H., *CRC Handbook of Chemistry and Physics*, 67th ed., CRC Press, Cleveland, OH, 1986-1987, pp. F-39-F-41.

[21]Tryggvason, G., "Numerical Simulation of the Rayleigh-Taylor Instability," *Journal of Computational Physics*, Vol. 75, April 1988, pp. 253-282.